Toward an orbital-free density functional theory of transition metals based on an electron density decomposition

Chen Huang
Department of Physics, Princeton University, Princeton, New Jersey 08544, USA

Emily A. Carter
Departments of Mechanical and Aerospace Engineering, Program in Applied and Computational Mathematics, and Andlinger Center for Energy and the Environment, Princeton University, Princeton, New Jersey 08544-5263, USA.

(Received 11 September 2011; revised manuscript received 16 December 2011; published 24 January 2012)

To properly apply approximate kinetic energy density functionals (KEDFs) used in orbital-free density functional theory (OF-DFT) to the highly inhomogeneous electron density in transition metals, we introduce a decomposition scheme in which the electron density is partitioned into delocalized and localized parts, which makes it possible to apply a different physically justifiable KEDF to each density. Using this decomposition scheme, we demonstrate that OF-DFT is able to quantitatively reproduce Kohn-Sham- (KS-)DFT predictions of the basic bulk properties of many phases of Ag, as well as surface energies, vacancy formation energies, and elastic moduli of face-centered-cubic Ag. However, OF-DFT Ag-Al alloy properties differ substantially from those predicted by KS-DFT using nonlocal pseudopotentials. These errors are due to remaining inaccuracies in the Ag and Al local electron-ion pseudopotentials, as well as the oversimplified model KEDF used for treating the interaction KE term between the localized and the delocalized electron densities. Future extensions to improve the treatment of transition metals are briefly outlined.

DOI: 10.1103/PhysRevB.85.045126 PACS number(s): 71.15.Mb, 71.15.Dx, 71.20.Be

I. INTRODUCTION

To fully understand many important phenomena in metals that happen at the length scale of nanometers or larger, for example, dislocation movement, grain boundary migration, and the unusually large yield strain in some amorphous metals,[1] fast yet accurate atomically-resolved simulation methods are needed. Although the use of classical interatomic potentials, e.g., the embedded atom method,[2] is much more computationally efficient than quantum-mechanics calculations, such classical simulations do not always produce reliable results. While much insight has been gleaned in many cases from such simulations, qualitatively incorrect predictions have been noted for, e.g., dislocation core structures in aluminum[3] and dislocation cross-slip in magnesium.[4] Another drawback with classical potential methods is that when the system contains many different elements, such as in complex metal alloys, it becomes difficult to fit the many cross terms in the potentials for many elements. Hence, it is appealing to consider whether quantum-mechanics methods, which, in principle, only require the input of atomic numbers of the elements, could be made fast enough to apply to the nanometer length scale and beyond.

At present, Kohn-Sham density functional theory (KS-DFT)[5,6] is the workhorse method for performing quantum-mechanics simulations of materials due to its attractive accuracy-cost trade-off. However, even faster quantum methods are needed, since conventional implementations of KS-DFT computations scale cubically with respect to the system size due to the need to orthogonalize all the occupied KS orbitals when solving the KS equations. Consequently, it becomes very expensive to apply conventional implementations of KS-DFT to systems containing more than a few hundred atoms. Of course, many linear-scaling KS-DFT methods have been introduced. Most of them either use localized bases for expanding the KS orbitals or solve locally truncated KS equations,[7] which makes these methods more appropriate for studying insulators in which the response function decays exponentially. However, for metals, these methods need more delocalized bases or much larger truncated regions due to the nonexponential decay of the response function in metallic systems. Furthermore, since KS-DFT calculations are still performed in these linear-scaling methods, they have a large prefactor in addition to their linear-scaling computational cost. In practice, as a result, these methods generally are not used for metals.

Orbital-free DFT (OF-DFT) is a promising method for performing linear scaling with low prefactor large-scale quantum-mechanics simulations for metals. In OF-DFT, the noninteracting electron kinetic energy DF (KEDF) of KS-DFT is expressed in terms of electron densities instead of KS orbitals. It already has been demonstrated that OF-DFT describes main group metals reasonably well,[8] with KS-DFT results as the benchmark. In practice, the same exchange-correlation (XC) functionals are employed in both OF-DFT and KS-DFT so that OF-DFT is, at best, an approximation to KS-DFT. In this paper, we offer a simple means to extend OF-DFT to transition-metal simulations as a step toward treating all metallic elements in the periodic table with OF-DFT.

When applying OF-DFT to transition metals, we face two main challenges. The first is the lack of good-quality local electron-ion pseudopotentials (LPSs) for transition metals. The nonlocal PSs (NLPSs) usually employed in KS-DFT, which typically involve orbital-based projection operators, cannot be used straightforwardly in OF-DFT due to the lack of an orbital representation. Even if good-quality LPSs have been built now for many main group elements,[9,10] it is not straightforward to rigorously extend our previous approach[9,10] to transition metals. In this paper, we discuss how to do so.

The second challenge is how to treat the highly inhomogeneous electron density (localized d electrons and delocalized sp electrons) in transition metals with approximate KEDFs. In a previous paper,[10] we showed that the asymptotic response behavior of KEDFs as $q \to 0$ in Fourier space was very different between insulators and metals. Consequently, it is very difficult to construct a versatile KEDF that works well simultaneously for both insulating and metallic systems, or localized and delocalized electron densities, since the physics of each is very different. To address this dichotomy, we introduce a simple electron density decomposition scheme in which the inhomogeneous electron density from transition metals is decomposed into delocalized and localized parts, to which different physically justifiable KEDFs then are applied to each component.

This paper is organized as follows. We first show how to build high-quality LPSs for transition metals and then describe our electron density decomposition scheme and the approximate KEDF we propose to use. We demonstrate the performance of OF-DFT here for the prototypical yet simple case of silver, a transition metal containing a closed d shell that is highly localized, by first calculating bulk properties for a variety of Ag phases. We then calculate elastic moduli, surface energies, and vacancy formation energies for the ground-state face-centered-cubic (FCC) Ag phase, as well as the potential energy curve of the Ag dimer, as further tests of the approach. We finally discuss OF-DFT results for hypothetical Ag-Al alloys, which points out remaining deficiencies in this simple scheme. We end with some thoughts on further refinements.

II. THEORY

A. Bulk-derived local pseudopotential for Ag

To build LPSs for transition metals, we should follow one basic rule: The lowest-energy eigenstate in a spherically symmetric potential well must have s angular momentum.[11] This can be shown briefly by noticing that, after a separation of variables, the Hamiltonian $\hat{H}$ becomes a radial function of the angular momentum l. Since $\partial \hat{H}[l]/\partial l > 0, l = 0$ gives the lowest energy according to the Hellmann-Feynman theorem.[12] However, taking Ag as an example, its $4d$ orbital has a lower eigenvalue than its $5s$ orbital. Therefore, we need to include Ag's $4s$ and $4p$ electrons as additional valence electrons. The importance of including $4s$ and $4p$ electrons in building a physical Ag LPS was not considered in the previous paper by Zhou and Carter.[13]

We build an Ag LPS based on its bulk electron density, i.e., the so-called bulk-derived LPS (BLPS).[9,14] The procedure is nearly the same as described in our previous paper.[9] Bulk valence-electron densities from three different bulk structures of Ag [FCC, body-centered cubic (BCC), and simple cubic (SC)] are obtained by performing KS-DFT calculations using an Ag NLPS (that acts only on Ag's $4d$ and $5s$ valence electrons) built using the FHI98 code[15] with default cutoff radii. Unlike our previous paper,[9] we also need Ag's $4s$ and $4p$ electron densities, which are prepared using a modified FHI98 code. The $4s$ and $4p$ all-electron orbitals are first pseudoized using the Troullier-Martins scheme,[16] with cutoff radii of 1.3 bohr (near the outer peaks of the $4s$ and $4p$ all-electron orbitals), before being superimposed with the NLPS bulk valence-electron densities to produce the final target bulk electron densities. The rest of the procedure is as reported earlier in Ref. 9: effective KS potentials are obtained by inverting the KS equations against these three target bulk electron densities, using the Wu-Yang optimized effective potential method.[17] The KS effective potentials then are unscreened by removing the Hartree and XC potentials. The unscreened KS potentials are Fourier transformed to Fourier space and then are divided by the bulk structure factors to obtain atom-centered potentials $\tilde{V}_{\mathrm{KS,atom}}(q)$. The three sets of data are used to construct the entire $\tilde{V}_{\mathrm{KS,atom}}(q)$. After adjusting the $\tilde{V}_{\mathrm{KS,atom}}(q)$ at the $q = 0$ point and the distance beyond which the Coulomb tail is enforced for $V_{\mathrm{KS,atom}}(r)$ in real space, we obtain the final Ag BLPS, shown in the inset of Fig. 1(a). For more details on the procedure for building BLPSs, please see Ref. 9.

B. Electron density decomposition

To apply a KEDF to the highly inhomogeneous electron density of transition metals, we introduce an electron density decomposition scheme. Again, we take the Ag atom as an example. We use KS-DFT with our Ag BLPS to calculate the electron density $\rho_{\mathrm{atom}}(r)$ (black solid curve in Fig. 1(a), having 19 electrons) for a single Ag atom. To decompose $\rho_{\mathrm{atom}}(r)$ into delocalized $\rho_{\mathrm{del}}(r)$ [red dash-dotted curve in Fig. 1(a)] and localized $\rho_{\mathrm{loc}}(r)$ [blue dashed curve in Fig. 1(a)] electron densities, we first choose a cutoff radius r_C that is small enough to prevent overlap between $\rho_{\mathrm{loc}}(r)$ from different Ag atoms in the structures studied in this paper. Beyond r_C, $\rho_{\mathrm{del}}(r)$ matches $\rho_{\mathrm{atom}}(r)$. Inside r_C, we select a point P at $r = 1.0$ bohr for interpolation, with its height to be adjusted. At the origin $r = 0$, $\rho_{\mathrm{del}}(r)$ is set to zero. We then perform a cubic spline interpolation using the origin, the point P, and the $\rho_{\mathrm{del}}(r)$ curve beyond r_C to construct the whole $\rho_{\mathrm{del}}(r)$. The height of the P point is determined by setting the integral of $\rho_{\mathrm{del}}(r)$ inside r_C to a predefined value $Q_{\mathrm{del}}^{r<r_C}$. $Q_{\mathrm{del}}^{r<r_C}$ is chosen in an *ad hoc* way. We want to have $Q_{\mathrm{del}}^{r<r_C}$ as small as possible to produce a fairly smooth $\rho_{\mathrm{del}}(r)$, to which an approximate KEDF designed for a nearly-free-electron gas is applied appropriately. However, $Q_{\mathrm{del}}^{r<r_C}$ also should be large enough to ensure that $\rho_{\mathrm{del}}(r)$ inside r_C is sufficient to represent any required change in electron density in that region during bond formation (even though such changes should be small anyway within r_C, since that region basically should be inert).[18] This flexibility is important, since we treat the localized electron density $\rho_{\mathrm{loc}}(r)$ on each Ag atom as frozen during the OF-DFT calculations.

To study the effect of r_C, we test three different r_C: 2.0, 2.2, and 2.4 bohr. To study $Q_{\mathrm{del}}^{r<r_C}$, we fix r_C at 2.2 bohr and test three different values for $Q_{\mathrm{del}}^{r<r_C}$: 2.0, 3.0, and 4.0. Detailed discussions on these parameters are presented later. In Fig. 1(a), we plot the delocalized electron density $\rho_{\mathrm{del}}(r)$ (red dash-dotted curve) calculated with $r_C = 2.2$ bohr and $Q_{\mathrm{del}}^{r<r_C} = 2.0$. The localized electron density (blue dashed curve) is obtained by subtracting $\rho_{\mathrm{del}}(r)$ from the total electron density $\rho_{\mathrm{atom}}(r)$ (black solid curve). In Fig. 1(b), we plot different $\rho_{\mathrm{del}}(r)$s calculated with different r_C and $Q_{\mathrm{del}}^{r<r_C}$ parameters. The delocalized electron density cannot be thought of as just

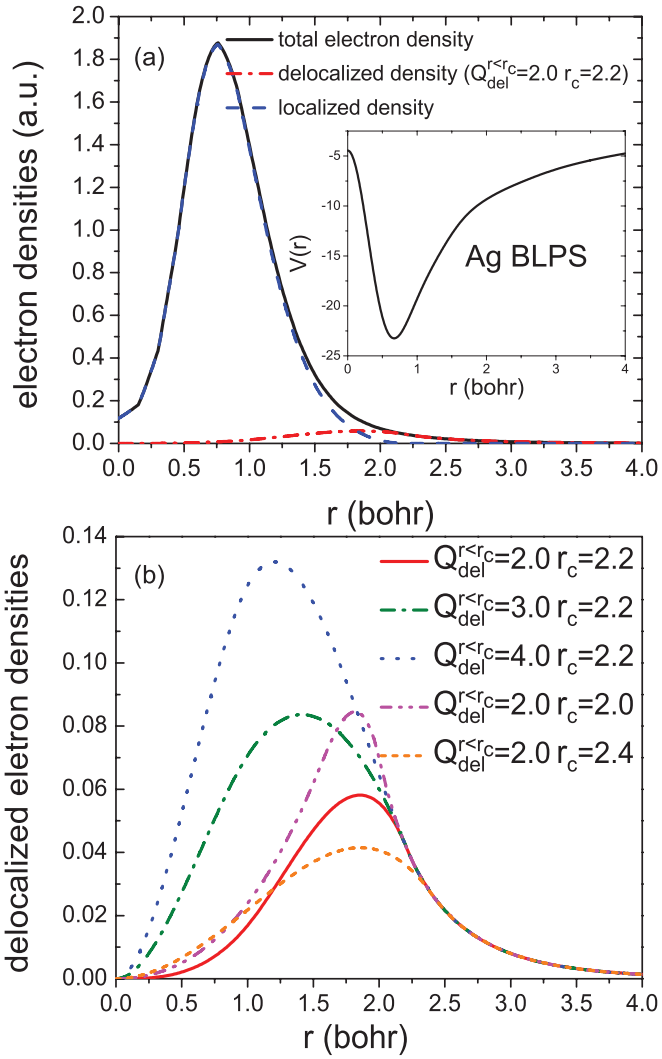

FIG. 1. (Color online) (a) Decomposition of the Ag atomic $4s^2 4p^6$ semicore plus $5s^1 4d^{10}$ valence-electron density (black solid curve, 19 electrons) into the delocalized electron density (red dash-dotted curve, using $Q_{del}^{r<r_C} = 2$ and $r_C = 2.2$ bohr) and the corresponding localized electron density (blue dashed curve). (Inset) Ag BLPS in real space. (b) Delocalized electron densities generated with different $Q_{del}^{r<r_C}$ and r_C parameters. With $r_C = 2.2$ bohr, the red solid curve is obtained with $Q_{del}^{r<r_C} = 2$, and the green dash-dotted and blue dotted curves are obtained with $Q_{del}^{r<r_C} = 3$ and $Q_{del}^{r<r_C} = 4$, respectively. With $Q_{del}^{r<r_C} = 2$, the pink dash-dot-dotted and orange dashed curves are obtained with $r_C = 2.0$ bohr and $r_C = 2.4$ bohr, respectively. All quantities are in Hartree atomic units.

the valence $5sp$ density, but it has contributions from the $4s$, $4p$, and valence $4d$ electrons as well.

In the cubic spline interpolation, the slope of $\rho_{del}(r)$ at $r = 0$ is set to zero to ensure that $\rho_{del}(r)$ can be expanded efficiently using a plane-wave basis set in later OF-DFT calculations. The slope of $\rho_{del}(r)$ is continuous across r_C, however we purposely let the curvature of $\rho_{del}(r)$ be discontinuous across r_C. For example, to the right of r_C in Fig. 1(a), the curvature of $\rho_{del}(r)$ is positive, equal to $\rho_{atom}(r)$. To the left of r_C, the curvature of $\rho_{del}(r)$ is negative to help $\rho_{del}(r)$ go to zero quickly. In practice, this discontinuity in the second derivative of the density at r_C causes no numerical difficulties or physical artifacts.

After the decomposition, the KE part of the DFT total energy functional is reformulated as

$$E_{tot}[\rho_{tot}] = T_s[\rho_{del}] + (T_s[\rho_{tot}] - T_s[\rho_{del}]) + E_{XC}[\rho_{tot}] + J[\rho_{tot}] + \int V_{ext}(\vec{r})\rho_{tot}(\vec{r})\, dr^3, \quad (1)$$

where the total electron density $\rho_{tot} = \rho_{del} + \rho_{loc}$. E_{XC}, J, $V_{ext}(\vec{r})$, and T_S are the XC energy, the Hartree energy, the external ionic potential (here, the BLPSs) energy, and the KS noninteracting KE. For the KE of the delocalized electron density, here we apply the nonlocal HC10 KEDF[10] with its parameter $\lambda = 0$ to the first $T_S[\rho_{del}]$ on the right-hand side of Eq. (1). The HC10 KEDF with $\lambda = 0$ is based on a single-electron-density-dependent kernel, and it describes well the nearly-free-electron gas, i.e., a delocalized electron density. Of course, other nonlocal KEDFs that describe the response of the nearly-free-electron gas well, such as the Wang-Teter[19] and the Wang-Govind-Carter[20] KEDFs, could have been used as well. The only other parameter β of the HC10 KEDF is set to 0.51, slightly larger than 0.5, to ensure that the KE potential is finite as the electron density goes to zero in vacuum regions.

Next, we discuss how to evaluate the $(T_S[\rho_{tot}] - T_S[\rho_{del}])$ term in Eq. (1). Here, we may use a local or semilocal KEDF,[21] which can be justified physically after reformulating this term as

$$(T_S[\rho_{tot}] - T_S[\rho_{del}]) = T_S[\rho_{loc}] + (T_S[\rho_{tot}] - T_S[\rho_{del}] - T_S[\rho_{loc}]). \quad (2)$$

Since ρ_{loc} is fixed in these OF-DFT calculations, $T_S[\rho_{loc}]$ is a constant once an approximate KEDF is chosen. The $(T_S[\rho_{tot}] - T_S[\rho_{del}] - T_S[\rho_{loc}])$ term in Eq. (2) is nothing but the interaction energy (the KE part) between the localized and the delocalized electron densities,[22] which we may approximate with local or semilocal KEDFs as has been done fruitfully in many previous embedding theories.[22] In this paper, we use a simple KEDF to represent the entire right-hand side of Eq. (2), a linear combination of Thomas-Fermi[23] (TF) and von Weizsäcker[24] (vW) KEDFs, i.e., $aT_{TF} + bT_{vW}$, where $T_{TF} = \frac{3}{10}(3\pi^2)^{2/3} \int \rho^{5/3}(\vec{r}) dr^3$ and $T_{vW} = \frac{1}{8} \int \frac{|\nabla\rho(\vec{r})|^2}{\rho(\vec{r})} dr^3$. The nonlinear correction to the delocalized density given in Eq. (2) can be thought of as a KE analog to the nonlinear core correction for XC functionals in the pseudopotential theory.[25] Thus, the correction of Eq. (2) may be thought of as providing the means to include the effect of the primarily d electrons on the delocalized (primarily sp) electrons.

III. NUMERICAL DETAILS

All KS-DFT calculations are performed using the ABINIT code.[26] The local density approximation[27] is used as the XC functional in all calculations, and a Fermi-Dirac smearing with a smearing width of 0.1 eV is used in all KS-DFT calculations. In this paper, KS-DFT calculations using the NLPS and the BLPS are labeled as KS-NLPS and KS-BLPS, respectively. OF-DFT calculations using the BLPS are labeled as OF-BLPS.

To build the Ag BLPS, FCC, BCC, and SC primitive cells are used. The plane-wave basis KE cutoff (E_{cut}) used for inverting the KS equations is 4000 eV with Monkhorst-Pack[28]

k-point meshes of $10 \times 10 \times 10$, $10 \times 10 \times 10$, and $8 \times 8 \times 8$ for FCC, BCC, and SC structures, respectively.

In all other KS-DFT calculations, E_{cut}s of 1200 and 2600 eV are used for KS-NLPS and KS-BLPS calculations, respectively, to converge the total energy to better than 1 meV per atom. The k mesh used is $14 \times 14 \times 14$ for FCC, hexagonal-close-packed (HCP), SC, and BCC Ag, and is $12 \times 12 \times 12$ for cubic diamond (CD) Ag. The FCC(100), FCC(110), and FCC(111) surfaces are modeled with five, seven, and five Ag FCC layers, respectively, with 10 Å vacuum in the surface normal direction to isolate periodic images of the surface slab in the supercell. The k-point mesh is $14 \times 14 \times 1$ in all FCC(110), FCC(111), and FCC(100) surface energy calculations. In vacancy formation energy calculations, eight FCC unit cells are padded in a $2 \times 2 \times 2$ way to form a supercell containing 32 atoms, with one Ag atom being removed to create a vacancy, and the k-point mesh used is $7 \times 7 \times 7$. In the Ag dimer calculations, a box of $10 \times 10 \times 20$ Å is used, with the long dimension being the one used to stretch the dimer bond.

OF-BLPS calculations are performed using a modified PROFESS 2.0 (Ref. 29) OF-DFT code, which uses a plane-wave basis. E_{cut} is set to 4000 eV to converge the total energy to 1 meV per atom in all OF-DFT calculations.

The elastic moduli for FCC Ag are obtained by fitting the primitive cell energy-versus-strain curves with parabolas. We directly calculate three basic elastic moduli, C_{11}, C_{44}, and C', by performing uniaxial, triaxial, and orthorhombic deformations, respectively. Here, for completeness, we give a brief description for how to compute them. For details, please read Ref. 30. The change in crystal energy under a small strain $\vec{e} = \{e_1,e_2,e_3,e_4,e_5,e_6\}$ is[30]

$$\Delta E = \frac{V}{2} \sum_{i=1}^{6} \sum_{j=1}^{6} C_{ij} e_i e_j,$$

where V is the equilibrium volume and C_{ij} are the elastic constants. For a cubic crystal, there are only three independent elastic constants due to its symmetry: C_{11}, C_{12}, and C_{44}. C_{11} can be calculated by applying a uniaxial strain $\vec{e} = \{\delta,0,0,0,0,0\}$. C_{44} is calculated with a triaxial strain $\vec{e} = \{0,0,0,\delta,\delta,\delta\}$. We do not calculate C_{12} here directly, but calculate C' directly with an orthorhombic strain $\vec{e} = \{\delta,\delta,(1+\delta)^{-2}-1,0,0,0\}$. C_{12} then is obtained as $C_{12} = (3B - 2C')/3$, where B is the bulk modulus. KS-DFT calculations for elastic moduli are performed with a k-point mesh of $20 \times 20 \times 20$.

To calculate properties of the hypothetical FCC alloys Ag_2Al_2, Ag_3Al, and $AgAl_3$, a cubic FCC unit cell is employed with four atoms. A k-point mesh of $14 \times 14 \times 14$ is used in the KS-DFT calculations. An Al BLPS generated in a previous paper[9] is used. The alloy formation energy is defined as $E_f = E_{\text{Ag}_n\text{Al}_m} - nE_{\text{Ag}} - mE_{\text{Al}}$, where E_{Ag} and E_{Al} are the energies per atom of bulk FCC Ag and bulk FCC Al and $E_{\text{Ag}_n\text{Al}_m}$ is the energy of the FCC four-atom cubic unit cell of the alloy.

IV. RESULTS AND DISCUSSION

A. Ag bulk phases

We first present results with the optimal parameters for the electron density decomposition: $Q_{\text{del}}^{r<r_C} = 2.0$ and $r_C = 2.2$ bohr. The electron density integrated beyond $r_C = 2.2$ bohr is 2.02; therefore, the total number of delocalized electrons Q_{del} is 4.02. In principle, if we could use the exact KEDF in Eq. (2) to compute the nonlinear correction to the KE of the delocalized electrons to account for the presence of the localized electrons, any choice of $Q_{\text{del}}^{r<r_C}$ and r_C would produce correct results, assuming that the HC10 KEDF yields an accurate KE for the delocalized electron density. In other words, our electron density decomposition method is formally exact. However, because in practice we need to calculate Eq. (2) using approximate KEDFs, e.g., the $aT_{\text{TF}} + bT_{\text{vW}}$ KEDFs employed here, we find that the particular choice of $Q_{\text{del}}^{r<r_C} = 2.0$ and $r_C = 2.2$ bohr gives the best description of all the Ag phases studied in this paper.

Table I displays both KS-DFT and OF-DFT data that allow us to assess the accuracy of both approximations in OF-DFT (the BLPS and the KEDF ansatz). The accuracy of our Ag BLPS is evidenced by the quantitative agreement we are able to achieve between KS-BLPS and KS-NLPS for properties of different Ag phases. Before embarking on OF-DFT calculations, we first must determine the two parameters in the $aT_{\text{TF}} + bT_{\text{vW}}$ KEDF used for evaluating Eq. (2). The parameters are fit to only two quantities: the KS-BLPS equilibrium energy and the bulk modulus for FCC Ag. We find the optimal a and b are 0.704 and 0.2175, respectively, coefficients that are similar in magnitude to the conventional gradient expansion (1 and 1/9). The equilibrium volume of FCC Ag and the bulk properties of other Ag phases are not used in the fitting, which makes them stringent tests of our decomposition scheme. Table I reveals that the OF-BLPS results agree very well with KS-BLPS predictions; this comparison evaluates errors engendered solely by our use of KEDFs. The OF-BLPS calculations even accurately reproduce the small energy difference between the HCP and the FCC phases. For total energies, the largest error using OF-BLPS compared to KS-BLPS is for CD Ag, with an error of 59 meV per atom, which actually is very small compared to the absolute energy difference between FCC and CD Ag.

TABLE I. Comparison of bulk moduli (B_0 in GPa), equilibrium volumes (V_0 in Å^3), and equilibrium energies (E_0 in eV) calculated by KS-NLPS, KS-BLPS, and OF-BLPS for different Ag phases. The electron density decomposition parameters used here are the optimal ones found: $Q_{\text{del}}^{r<r_C} = 2.0$ and $r_C = 2.2$, while the $aT_{\text{TF}} + bT_{\text{vW}}$ coefficients were fit only to the KS-BLPS B_0 and E_0 of FCC Ag with the optimal values $a = 0.704$ and $b = 0.2175$. The absolute energies for FCC Ag are shown. For other phases, their relative energies with respect to FCC Ag are given.

		FCC	HCP	BCC	SC	CD
B_0	KS-NLPS	133	131	127	102	50
	KS-BLPS	134	134	129	91	51
	OF-BLPS	139	137	130	88	53
V_0	KS-NLPS	16.342	16.377	16.447	18.647	26.960
	KS-BLPS	16.432	16.448	16.545	18.756	26.286
	OF-BLPS	15.706	15.701	15.962	19.066	26.837
E_0	KS-NLPS	−985.953	0.008	0.045	0.399	1.034
	KS-BLPS	−3937.174	0.003	0.021	0.286	0.812
	OF-BLPS	−3937.164	0.005	0.065	0.310	0.753

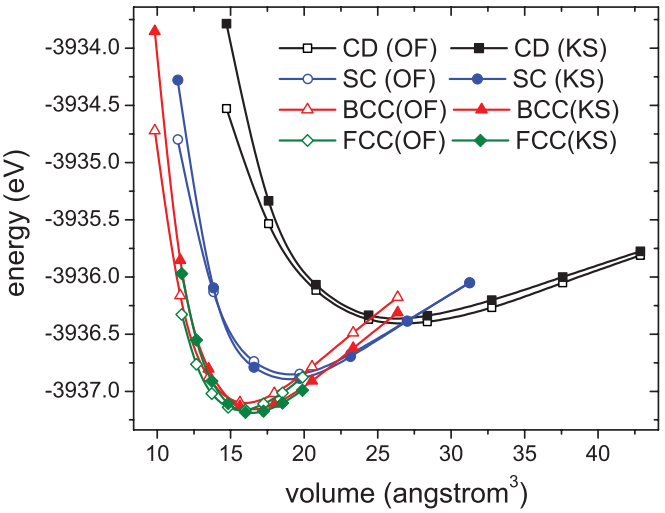

FIG. 2. (Color online) Comparison of the OF-BLPS and KS-BLPS energy-versus-volume curves for FCC, BCC, SC, and CD Ag over a wide range of volumes. KS-BLPS results are in filled symbols, and OF-BLPS results are in open symbols.

For bulk moduli, OF-BLPS results agree with KS-BLPS with a maximum error of 5 GPa, which is a <5% deviation in all cases. For equilibrium volumes, the error of the OF-BLPS scheme compared to KS-BLPS again is small: ∼ 4.6%, 4.7%, and 3.3% for FCC, HCP, and BCC Ag, respectively. Figure 2 also displays the overall agreement between the KS-BLPS and the OF-BLPS calculations for FCC, BCC, SC, and CD Ag over a wide range of volumes.

We also examined the sensitivity of predicted bulk properties of Ag to the use of different electron density decompositions (characterized by $Q_{\rm del}^{r<r_C}$ and r_C). For each set of $Q_{\rm del}^{r<r_C}$ and r_C, coefficients a and b in $aT_{\rm TF}+bT_{\rm vW}$ were refit to reproduce the KS-DFT bulk modulus and equilibrium energy of FCC Ag. First, we consider the cases with different $Q_{\rm del}^{r<r_C}$ by fixing r_C at 2.2 bohr. In Table II, $Q_{\rm del}^{r<r_C}=3$ and $Q_{\rm del}^{r<r_C}=4$ give smaller, less accurate bulk moduli than the $Q_{\rm del}^{r<r_C}=2$ case (see Table I). Both $Q_{\rm del}^{r<r_C}=3$ and $Q_{\rm del}^{r<r_C}=4$ give smaller, less accurate volumes than the $Q_{\rm del}^{r<r_C}=2$ case (see Table I). Upon increasing $Q_{\rm del}^{r<r_C}$, the energy differences between FCC Ag and the low-coordination-number structures (BCC, SC, and CD Ag) decrease too much. For $Q_{\rm del}^{r<r_C}=4$, HCP, BCC, SC, and CD Ag even have lower energies than FCC Ag.

To consider the effect of the cutoff radius r_C, we tested $r_C=2.0$ bohr and $r_C=2.4$ bohr, fixing $Q_{\rm del}^{r<r_C}=2.0$. Table II shows that $r_C=2.4$ bohr generally gives better results than the case of $r_C=2.0$ bohr. The total delocalized electrons $Q_{\rm del}$ are 4.62 and 3.57 for $r_C=2.0$ bohr and $r_C=2.4$ bohr, respectively. The better results obtained by $r_C=2.4$ bohr can be attributed to its more accurate nonlinear correction [Eq. (2)] to the KE, because with $r_C=2.4$ bohr, we obtain a much softer delocalized electron density [orange dashed curve in Fig. 1(b)] than the case of $r_C=2.0$ bohr [pink dash-dot-dotted curve in Fig. 1(b)]. Because we employ the linear combination of TF and vW KEDFs to approximate Eq. (2), we need to choose a proper $Q_{\rm del}^{r<r_C}$ and r_C to generate soft delocalized electron densities in order to make the approximation to Eq. (2) more accurate. This also explains why $Q_{\rm del}^{r<r_C}=3$ gives better results than $Q_{\rm del}^{r<r_C}=4$ in the previous test. Here, $Q_{\rm del}^{r<r_C}=3$ gives a much softer delocalized electron density [green dash-dotted curve in Fig. 1(b)] than the case of $Q_{\rm del}^{r<r_C}=4$ [blue dotted curve in Fig. 1(b)]. By softer, we mean more delocalized. Since the dominant term in our TF + vW functional is TF, which is exact for the uniform electron gas, the less sharply structured the density is, the more accurate the evaluation of the nonlinear KEDF correction will be.

Two further tests of the selected density decomposition and KE evaluation were performed. In the first test, all 19 electrons in our Ag pseudoatom are considered as delocalized electrons in FCC Ag and are treated with the HC10 KEDF. We find that the energy-versus-volume curve simply keeps decreasing as the volume expands and essentially, unphysically yields essentially no bound state, highlighting the need for a

TABLE II. Basic bulk properties for several Ag phases based on different electron density decomposition parameters $Q_{\rm del}^{r<r_C}$ and r_C. Cutoff radii r_C are in bohr. Bulk moduli (B_0) are in GPa. Equilibrium volumes (V_0) and energies (E_0) are in Å^3 and eV, respectively. Results obtained using $Q_{\rm del}^{r<r_C}=2.0$ and $r_C=2.2$ and without the use of a nonlinear correction to KE in Eq. (2) are labeled "$Q_{\rm del}^{r<r_C}=2.0$ (no $\rho_{\rm loc}$)".

		FCC	HCP	BCC	SC	CD
$Q_{\rm del}^{r<r_C}=3.0$	B_0	135	135	122	83	42
$r_C=2.2$	V_0	14.032	14.039	14.214	17.111	22.919
	E_0	−3937.163	−0.006	0.032	0.091	0.334
$Q_{\rm del}^{r<r_C}=4.0$	B_0	134	89	108	53	25
$r_C=2.2$	V_0	14.224	14.124	14.175	16.938	22.681
	E_0	−3937.181	−0.002	−0.008	−0.178	−0.160
$Q_{\rm del}^{r<r_C}=2.0$	B_0	5234	4624	3681	1802	843
(no $\rho_{\rm loc}$)	V_0	4.790	4.837	4.885	6.721	10.133
	E_0	−5078.392	0.211	1.443	3.855	5.096
$Q_{\rm del}^{r<r_C}=2.0$	B_0	136	142	128	108	46
$r_C=2.0$	V_0	14.418	14.382	14.549	17.006	23.124
	E_0	−3937.168	−0.014	0.020	0.055	0.561
$Q_{\rm del}^{r<r_C}=2.0$	B_0	139	140	123	83	43
$r_C=2.4$	V_0	16.132	16.186	16.491	19.458	28.300
	E_0	−3937.166	0.012	0.097	0.507	1.041

TABLE III. Comparison of FCC Ag elastic moduli (in GPa) C_{11}, C', and C_{44} among KS-NLPS, KS-BLPS, and OF-BLPS. C_{12} is calculated via the formula: $(3B - 2C')/3$, where B is the bulk modulus taken from the corresponding values in Table I.

	C_{11}	C_{44}	C'	C_{12}
KS-NLPS	162	61	22	118
KS-BLPS	160	47	18	122
OF-BLPS	185	64	27	121

separate treatment of the KEs of localized and delocalized electron densities. In the second test, we set $Q_{\rm del}^{r<r_C} = 2$ and do not employ the nonlinear correction [Eq. (2)] to the KE that accounts for the presence of the localized electrons. These results are labeled as "$Q_{\rm del}^{r<r_C} = 2.0$ (no $\rho_{\rm loc}$)" in Table II. Here, the equilibrium volumes and energies are far too small (too negative), and the bulk moduli are far too large compared to the KS-DFT values (in Table I), indicating the crucial importance of the nonlinear KEDF correction term. These large discrepancies between OF-DFT and KS-DFT that occur when ignoring the nonlinear KE correction are due to the neglect of the repulsion from the localized electrons.

B. Elastic moduli of FCC Ag

Accurate predictions of elastic moduli are among the most important properties to reproduce when performing simulations of mechanical properties of materials. Here, we calculate elastic moduli for FCC Ag. Table III provides comparisons that isolate the error of the BLPS as well as that of the KEDF scheme. By comparing KS-NLPS and KS-BLPS results, we find the Ag BLPS produces a maximum error of 14 GPa for the C_{44} (~23% deviation). We also see that our electron density decomposition scheme works fairly well for elastic moduli: OF-BLPS results are in fair agreement with those of KS-BLPS with a maximum error of 25 GPa (<16% deviation) for C_{11}. Furthermore, Figs. 3–5 display overall quite good agreement between the OF-BLPS and the KS-BLPS elastic behavior over a wide range of strains. While these deviations of ~20% may sound large, it is important to recall that no OF-DFT calculation has ever even be able to produce an energy minimum properly for bulk Ag, let alone reasonable moduli, so our current scheme is a vast improvement over earlier attempts.[13]

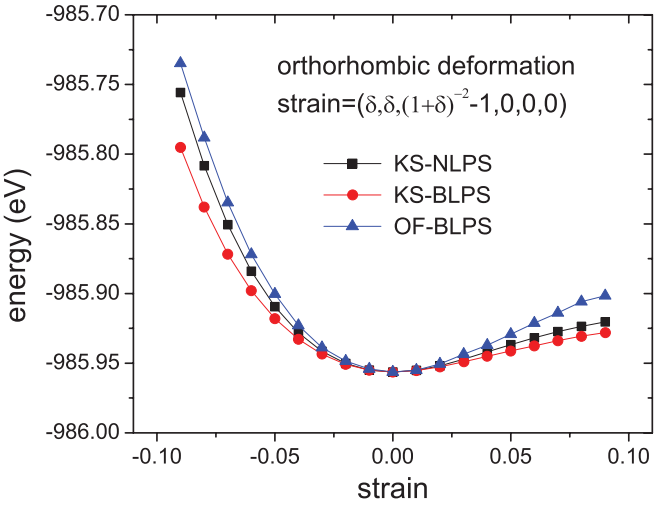

FIG. 4. (Color online) Orthorhombic deformation of FCC Ag. Comparison of the energy-versus-strain (δ) curves from KS-NLPS, KS-BLPS, and OF-BLPS. The applied strain is $\vec{e} = (\delta,\delta,(1+\delta)^{-2} - 1,0,0,0)$. The KS-BLPS and OF-BLPS curves are shifted to match the KS-NLPS curve at zero strain.

C. Ag dimer, surface energies, and vacancy formation energies

Since the Ag BLPS is built based on bulk electron densities and, thus far OF-DFT has been more applicable

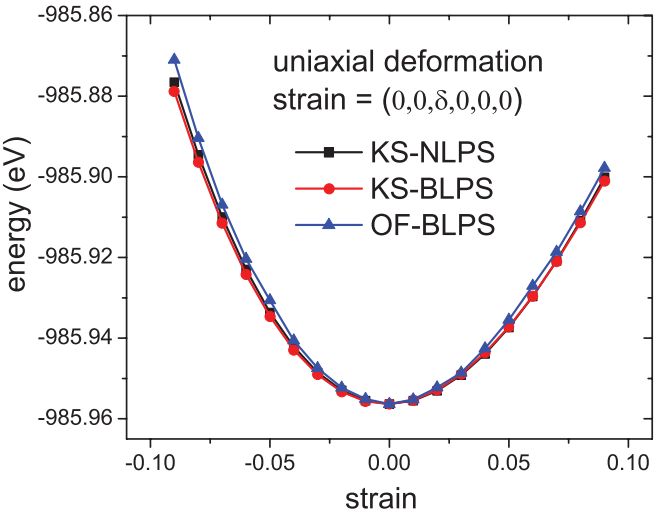

FIG. 3. (Color online) Uniaxial deformation of FCC Ag. Comparison of the energy-versus-strain (δ) curves among KS-NLPS, KS-BLPS, and OF-BLPS. The applied strain is $\vec{e} = (0,0,\delta,0,0,0)$. The KS-BLPS and OF-BLPS curves are shifted to match the KS-NLPS curve at zero strain.

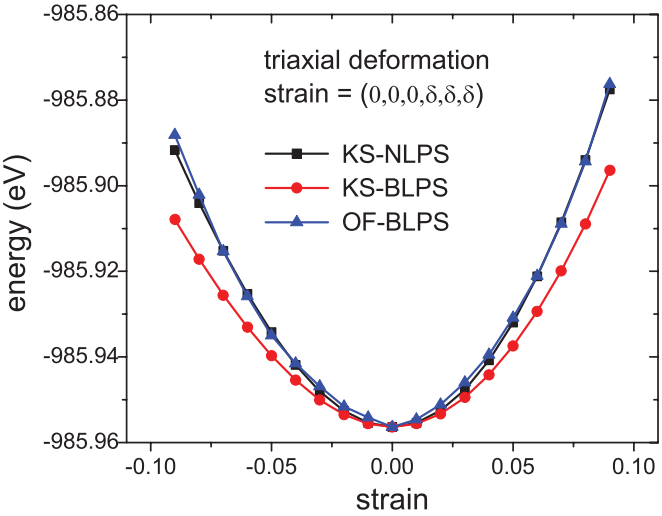

FIG. 5. (Color online) Triaxial deformation of FCC Ag. Comparison of the energy-versus-strain (δ) curves from KS-NLPS, KS-BLPS, and OF-BLPS. The applied strain is $\vec{e} = (0,0,0,\delta,\delta,\delta)$. The KS-BLPS and OF-BLPS curves are shifted to match the KS-NLPS curve at zero strain.

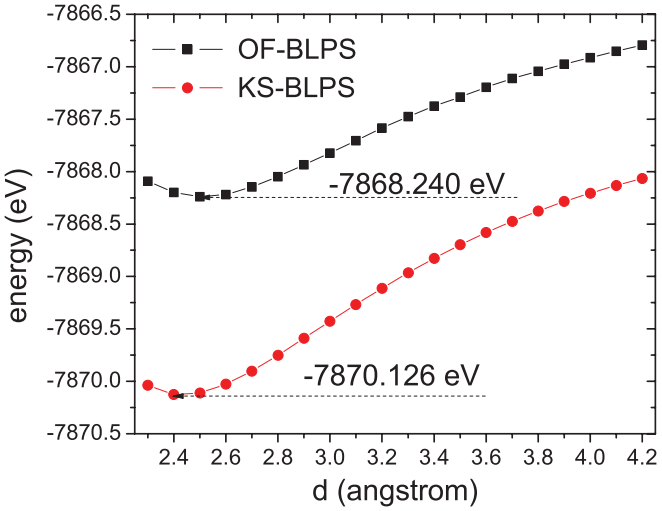

FIG. 6. (Color online) The total energy versus the bond length for the Ag dimer, calculated using OF-BLPS and KS-BLPS. The minima of the two curves are labeled.

to condensed matter, here we challenge the Ag BLPS and our electron density decomposition scheme for the KE by calculating the binding energy curve of the Ag dimer as well as surface energies and vacancy formation energies for FCC Ag. In all these calculations, we use the previously obtained optimal parameters for evaluating Eq. (2): $a = 0.704$ and $b = 0.2175$.

For the Ag dimer (Fig. 6), we find that OF-BLPS total energy is consistently higher than KS-BLPS: The minima of the two curves differ by 1.896 eV, which is a large error. However, the equilibrium bond lengths from OF-BLPS and KS-BLPS are fairly close: 2.51 Å from the OF-BLPS and 2.42 Å from the KS-BLPS. Also encouraging is that the curves are reasonably parallel to one other. The large error is attributed to (1) use of the HC10 KEDF (with $\lambda = 0$) that is meant to work well for a nearly-free-electron gas (which the dimer clearly is not) and (2) the oversimplified model, i.e., the linear combination of TF and vW KEDFs, for evaluating Eq. (2).

Table IV shows that KS-NLPS surface energies are ∼200–300 mJ/m^2 higher than the KS-BLPS results, which indicates the level of error associated just with the Ag BLPS when used for open structures, such as surfaces. The OF-BLPS surface energies are consistently ∼200 mJ/m^2 higher than the KS-BLPS results, which fortuitously brings them into closer agreement with the conventional KS-NLPS predictions, including giving the correct ordering of the surface energies.

TABLE IV. Comparison of surface energies (in mJ/m^2) and vacancy formation energies (E_{vf} in eV) among KS-NLPS, KS-BLPS, and OF-BLPS.

	FCC(111)	FCC(100)	FCC(110)	E_{vf}
KS-NLPS	1103	1224	1329	1.17
KS-BLPS	826	1005	1075	0.87
OF-BLPS	1064	1200	1337	0.95

TABLE V. Comparison of alloy formation energies (E_f in eV), bulk moduli (B_0 in GPa), and equilibrium volumes (V_0 in Å^3) between Ag and Al, calculated using KS-NLPS, KS-BLPS, and OF-BLPS.

		B_0	V_0	E_f
$AgAl_3$	KS-NLPS	93	63.714	0.13
	KS-BLPS	67	65.932	−0.61
	OF-BLPS	69	65.476	−0.47
Ag_2Al_2	KS-NLPS	108	63.426	−0.15
	KS-BLPS	76	66.790	−1.02
	OF-BLPS	78	66.121	−0.65
Ag_3Al	KS-NLPS	128	63.616	−0.36
	KS-BLPS	101	65.733	−0.96
	OF-BLPS	94	64.813	−0.48

This 200 mJ/m^2 is equivalent to about 0.1 eV per surface-layer atom after we convert this 200 mJ/m^2 error to the energy errors associated with the surface-layer atoms. The vacancy formation energy also is reproduced well by the OF-BLPS scheme (Table IV): 0.95 eV compared to 0.87 eV from KS-BLPS. As KS-NLPS predicts 1.17 eV, some of the error is again attributable to the Ag BLPS.

D. Alloy formation energies

Last, we calculate hypothetical Ag-Al alloy formation energies as well as their equilibrium volumes and bulk moduli, using the KS-NLPS, KS-BLPS, and OF-BLPS schemes. Alloys provide a severe test of the transferability of our approach. Table V shows that the KS-BLPS and OF-BLPS methods give bulk moduli that are too small with a maximum error of ∼30 GPa (∼30% deviation) compared to the KS-NLPS benchmarks. However, the KS-BLPS and OF-BLPS results are close, which suggests the error is due to the Ag and Al BLPSs, which may not have the flexibility to describe charge transfer between Ag and Al properly. For the equilibrium volumes, again KS-BLPS and OF-BLPS results are close; however, the differences between KS-BLPS and KS-NLPS are large, with a maximum error of ∼5% for the Ag_2Al_2 case. The KS-BLPS and KS-NLPS also give quite different alloy formation energies. All of these errors are due to inaccuracies in the Ag and Al BLPSs. We do see that the ordering of the alloy formation energies is reproduced correctly by OF-DFT (comparing OF-BLPS to KS-BLPS), but the alloy formation energies between KS-BLPS and OF-BLPS are quite different, which indicates that our oversimplified model, the linear combination between TF and vW KEDFs for evaluating Eq. (2), needs to be improved further.

V. CONCLUSIONS

In this paper, we demonstrated a step forward in extending the range of materials that OF-DFT may reliably simulate, namely to the treatment of transition metals. We tried to solve two prominent challenges: (1) the lack of good-quality LPSs for transition metals and (2) the difficulty in applying KEDFs to the inhomogeneous d electrons. For the first problem, we emphasized the importance of having the s

angular momentum channel as the lowest-energy eigenstate for building a physically reasonable LPS. Our Ag BLPS then was shown to work well if the system contained pure Ag. However, Ag-Al alloy properties calculated using Ag and Al BLPSs are substantially different from the NLPS results, which indicates further improvement of LPSs is needed. To build better LPSs, schemes that yield LPSs to explicitly reproduce the all-electron atomic eigenvalues, as proposed by Starkloff and Joannopoulos,[11] are worth exploring, as they may do a better job of describing charge transfer between elements.

To tackle the second problem, we proposed a simple electron density decomposition scheme in which the inhomogeneous electron density was decomposed into localized and delocalized parts. For each part, we applied a physically justified KEDF. We demonstrated this scheme by calculating bulk properties for different Ag phases, Ag dimer, and the surface and vacancy formation energies of FCC Ag. With an optimal electron density decomposition, except for the Ag dimer case, OF-BLPS was in quantitative agreement with KS-BLPS, which validated our decomposition scheme. Moreover, elastic deformations and elastic moduli were reproduced fairly well. However, large quantitative errors were encountered for alloy bulk properties, which were due to both deficiencies in the LPSs and the oversimplified model for treating the interaction KE in Eq. (2). Ongoing work considers other hybrid schemes for treating localized and delocalized density contributions to the KE as well as introducing nonlocality into the electron-ion term.[31]

In conclusion, we have demonstrated a route to extend OF-DFT to treat transition metals. Together with the already good performance of OF-DFT for treating main group metals, OF-DFT becomes promising for performing accurate and relatively fast large-scale quantum-mechanics simulations for metals beyond the main group in the periodic table. Important applications should someday include amorphous metals, mechanical properties of nanocrystalline metals, and warm dense matter containing transition metals, to name only a few.

ACKNOWLEDGMENTS

We are grateful to the Office of Naval Research and the National Science Foundation for support of this work, as well as to Dr. Youqi Ke, Junchao Xia, and Dr. Florian Libisch for many helpful discussions.

APPENDIX: AN IMPROVED INTERPOLATION METHOD FOR THE HC10 KEDF

In this paper, the HC10 KEDF is evaluated with an improved interpolation scheme. We first interpolate the nonlocal KEDF kernel in real space, using Hermite polynomials as

$$\begin{aligned} T_{NL}[\rho] &= \iint \rho^{\alpha}(\vec{r})\omega[\xi(\vec{r})|\vec{r}-\vec{r}'|]\rho^{\beta}(\vec{r}')dr^3dr'^3 \\ &= \iint \rho^{\alpha}(\vec{r})\sum_{j=1}\theta[\xi(\vec{r})-\xi_j]\theta[\xi_{j+1}-\xi(\vec{r})] \\ &\quad\times\left(h_{00}(t_j)\omega_j + h_{10}(t_j)h_j\left.\frac{\partial\omega}{\partial\xi}\right|_{\xi_j}\right. \\ &\quad + h_{01}(t_j)\omega_{j+1} + h_{11}(t_j)h_j\left.\frac{\partial\omega}{\partial\xi}\right|_{\xi_{j+1}}\right)\rho^{\beta}(\vec{r}')dr^3dr'^3. \end{aligned} \tag{A1}$$

Above, $\omega[\xi(\vec{r})|\vec{r}-\vec{r}'|]$ is the kernel of the HC10 nonlocal KEDF defined in Ref. 10. $\theta[\xi(\vec{r})-\xi_j]$ is the Heaviside step function. The bins $\{\xi_j\}$ cover the whole range of $\xi(\vec{r})$ in real space, and they form a geometric sequence with the binning ratio defined as $b=\xi_{j+1}/\xi_j$. ω_j is the kernel evaluated at ξ_j. $\left.\frac{\partial\omega}{\partial\xi}\right|_{\xi_j}$ is the derivative of the kernel with respect to $\xi(\vec{r})$, evaluated at ξ_j. The other variables are defined as

$$\begin{aligned} h_j &= \xi_{j+1}-\xi_j, \\ t_j(\vec{r}) &= [\xi(\vec{r})-\xi_j]/h_j. \end{aligned}$$

The cubic Hermite interpolation in Eq. (A1) is defined using the Hermite polynomial basis,

$$\begin{aligned} h_{00}(t) &= 2t^3-3t^2+1, \\ h_{10}(t) &= t^3-2t^2+t, \\ h_{01}(t) &= -2t^3+3t^2, \\ h_{11}(t) &= t^3-t^2. \end{aligned}$$

In practice, the binning ratio b is small enough to converge the OF-DFT total energy to better than 1 meV per atom. The KE potential is obtained by performing the functional derivative of Eq. (A1) with respect to the electron density, therefore the KE potential is always consistent with the KE, which is a great improvement over our previous approach,[10] in which the KE potential and the KE are computed separately and are not guaranteed to be consistent with each other, unless each of them is calculated highly accurately.

[1] J. Das, M. B. Tang, K. B. Kim, R. Theissmann, F. Baier, W. H. Wang, and J. Eckert, Phys. Rev. Lett. **94**, 205501 (2005).
[2] M. S. Daw and M. I. Baskes, Phys. Rev. B **29**, 6443 (1984).
[3] C. Woodward, D. R. Trinkle, L. G. Hector Jr., and D. L. Olmsted, Phys. Rev. Lett. **100**, 045507 (2008).
[4] I. Shin and E. A. Carter, Modelling Simul. Mater. Sci. Eng. **20**, 015006 (2012).
[5] W. Kohn and L. J. Sham, Phys. Rev. **140**, A1133 (1965).
[6] P. Hohenberg and W. Kohn, Phys. Rev. **136**, B864 (1964).
[7] S. Goedecker, Rev. Mod. Phys. **71**, 1085 (1999).
[8] E. Smargiassi and P. A. Madden, Phys. Rev. B **51**, 117 (1995); B. J. Jesson and P. A. Madden, J. Chem. Phys. **113**, 5924 (2000); K. M. Carling and E. A. Carter, Modell. Simul. Mater. Sci. Eng. **11**, 339 (2003); G. Ho, M. T. Ong, K. J. Caspersen, and E. A. Carter, Phys. Chem. Chem. Phys. **9**, 4951 (2007); G. Ho, C. Huang, and E. A. Carter, Curr. Opin. Solid State Mater. Sci. **11**, 57 (2008);

I. Shin, A. Ramasubramaniam, C. Huang, L. Hung, and E. A. Carter, Philos. Mag. **89**, 3195 (2009).
[9]C. Huang and E. A. Carter, Phys. Chem. Chem. Phys. **10**, 7109 (2008).
[10]C. Huang and E. A. Carter, Phys. Rev. B **81**, 045206 (2010).
[11]T. Starkloff and J. D. Joannopoulos, Phys. Rev. B **16**, 5212 (1977).
[12]H. Hellmann, *Einführung in die Quantenchemie* (Franz Deuticke, Leipzig, 1937), Sec. 54; R. P. Feynmann, Phys. Rev. **56**, 340 (1939).
[13]B. Zhou and E. A. Carter, J. Chem. Phys. **122**, 184108 (2005).
[14]B. Zhou, Y. A. Wang, and E. A. Carter, Phys. Rev. B **69**, 125109 (2004).
[15]M. Fuchs and M. Scheffler, Comput. Phys. Commun. **119**, 67 (1999).
[16]N. Troullier and J. L. Martins, Phys. Rev. B **43**, 1993 (1991).
[17]Q. Wu and W. T. Yang, J. Chem. Phys. **118**, 2498 (2003).
[18]S. Goedecker and K. Maschke, Phys. Rev. A **45**, 88 (1992).
[19]L.-W. Wang and M. P. Teter, Phys. Rev. B **45**, 13196 (1992).
[20]Y. A. Wang, N. Govind, and E. A. Carter, Phys. Rev. B **60**, 16350 (1999); **64**, 089903(E) (2001).
[21]A. J. Thakkar, Phys. Rev. A **46**, 6920 (1992).
[22]G. Senatore and K. R. Subbaswamy, Phys. Rev. B **34**, 5754 (1986); P. Cortona, *ibid.* **44**, 8454 (1991); T. A. Wesolowski and A. Warshel, J. Phys. Chem. **97**, 8050 (1993); N. Govind, Y. A. Wang, and E. A. Carter, J. Chem. Phys. **110**, 7677 (1999).
[23]L. H. Thomas, Proc. Cambridge Philos. Soc. **23**, 542 (1927); E. Fermi, Rend. Acad. Naz. Lincei **6**, 602 (1927); Z. Phys. **48**, 73 (1928).
[24]C. F. v. Weizsäcker, Z. Phys. **96**, 431 (1935).
[25]S. Louie, S. Froyen, and M. L. Cohen, Phys. Rev. B **26**, 1738 (1982).
[26]X. Gonze, B. Amadon, P. Anglade, J.-M. Beuken, F. Bottin, P. Boulanger, F. Bruneval, D. Caliste, R. Caracas, M. Côté, T. Deutsch, L. Genovese, P. Ghosez, M. Giantomassi, S. Goedecker, D. Hamann, P. Hermet, F. Jollet, G. Jomard, S. Leroux, M. Mancini, S. Mazevet, M. Oliveira, G. Onida, Y. Pouillon, T. Rangel, G.-M. Rignanese, D. Sangalli, R. Shaltaf, M. Torrent, M. Verstraete, G. Zerah, and J. Zwanziger, Comput. Phys. Commun. **180**, 2582 (2009).
[27]J. P. Perdew and A. Zunger, Phys. Rev. B **23**, 5048 (1981).
[28]H. J. Monkhorst and J. D. Pack, Phys. Rev. B **13**, 5188 (1976).
[29]G. Ho, V. L. Ligneres, and E. A. Carter, Comput. Phys. Commun. **179**, 839 (2008); L. Hung, C. Huang, I. Shin, G. Ho, V. L. Ligneres, and E. A. Carter, *ibid.* **181**, 2208 (2010).
[30]S. Q. Wang and H. Q. Ye, J. Phys.: Condens. Matter **15**, 5307 (2003).
[31]Y. Q. Ke and E. A. Carter (to be published).